photonics

MDPI

Article

Fiber Laser Induced Breakdown Spectroscopy Combined with Surface Enhancement and Spark Discharge for Sensitive Detection of Heavy Metals in Hair Dye Creams

Shudi Zhang [1,*], Jianyun Lin [1], Jingru Huang [1], Zhisen Liang [2], Fangfang Chen [1] and Guihong Wang [1]

[1] Engineering Research Center of Natural Cosmeceuticals College of Fujian Province, School of Public Health and Medical Technology, Xiamen Medical College, Xiamen 361023, China; linjian1@xmmc.edu.cn (J.L.); huangjingru1@xmmc.edu.cn (J.H.); cff@xmmc.edu.cn (F.C.); wgh@xmmc.edu.cn (G.W.)

[2] Guangzhou Inspection, Testing and Certification Group Co., Ltd., Guangzhou 511447, China; 18805065173@163.com

* Correspondence: zsd@xmmc.edu.cn

Abstract

The unauthorized addition of silver nitrate and excessive heavy metals in hair dye creams poses serious health risks, creating an urgent need for rapid and sensitive detection methods. In this study, a spark discharge-enhanced fiber laser-induced breakdown spectroscopy (SD-LIBS) system was developed for the simultaneous detection of five heavy metal ions (Ag, Pb, Cd, As, Hg) in hair dye creams. The system combines three signal enhancement strategies: high-voltage spark discharge, Au nanoparticle-assisted enhancement, and analyte enrichment on a superhydrophobic–hydrophilic patterned graphite substrate. Hydrophilic micro-pits were fabricated by laser scanning on the superhydrophobic graphite surface to confine and concentrate analyte residues upon droplet drying. Under optimized discharge conditions of 22 nF and 2000 V, the spark discharge achieved a signal-to-noise ratio enhancement of approximately 12 times. Au nanoparticle enhancement further increased the signal intensity by 49.3%. The optimal pit diameter and sample loading volume were 0.1 mm and 30 μL, respectively. The calibration curves for all five elements showed good linearity with R^2 values close to 0.99, and the lowest detection limits reached 1.9 μg/L for Ag. The average spiked recovery was 82.07%. The method was applied to four commercial hair dye cream samples, and the Ag detection results agreed well with ICP-OES reference values with an average error of 16.41%. This work demonstrates that the proposed SD-LIBS system offers a low-cost, rapid, and sensitive approach for on-site screening of heavy metals in cosmetics and other consumer products.

Keywords: laser-induced breakdown spectroscopy; fiber laser; spark discharge; heavy metals; hair dye cream; superhydrophobic surface; gold nanoparticles

Check for updates

Received: 22 July 2026
Revised: 20 August 2026
Accepted: 26 August 2026
Published: 1 September 2026

Copyright: © 2026 by the authors. Licensee MDPI, Basel, Switzerland. This article is an open access article distributed under the terms and conditions of the Creative Commons Attribution (CC BY) license.

1. Introduction

The global cosmetics industry has grown steadily over the past two decades, and hair dye creams are one of the fastest-growing product categories. With this growth, heavy metal contamination in cosmetics has become a serious public health concern, because long-term skin contact can lead to gradual absorption and buildup of toxic metals in the body [1]. One key problem is the unauthorized use of silver nitrate in some hair dye creams as a quick blackening agent. Silver ions bind to sulfur-containing amino acids in keratin and then get oxidized in air to form black silver sulfide (Ag_2S), which darkens the hair

immediately. But silver nitrate is strongly corrosive and toxic. Long-term skin contact can cause burns, argyria (a condition where the skin turns blue–gray permanently), and damage to the liver and kidneys [2]. China's Cosmetic Safety and Technical Specification (2015) allows silver nitrate only for eyelash and eyebrow products, banning it from hair products entirely. The same regulation also sets strict limitson lead (Pb $\leq$ 10 mg/kg), arsenic (As $\leq$ 2 mg/kg), mercury (Hg $\leq$ 1 mg/kg), and cadmium (Cd $\leq$ 5 mg/kg), which are known to cause cancer, nerve damage, and kidney problems [1]. Other major markets have similar restrictions. The EU Cosmetics Regulation [3] lists silver nitrate in Annex II as a prohibited substance, and the German BVL (2016) established technically unavoidable level limits for heavy metal impurities, including Pb $\leq$ 2.0 mg/kg (5.0 mg/kg for powders, lipsticks, and eye shadows), As $\leq$ 0.5 mg/kg, Cd $\leq$ 0.1 mg/kg, and Hg $\leq$ 0.1 mg/kg. In the U.S., the FDA permits silver nitrate only as a color additive for professional-use eyebrow and eyelash coloring at up to 4% (21 CFR 73.2550), and mercury in cosmetics is limited to 1 mg/kg (21 CFR 700.13), with a non-binding guidance recommending 10 ppm lead in lip products and externally applied cosmetics. Therefore, there is a clear need for a fast, sensitive, and affordable method to detect silver and other heavy metals in hair dye creams at the same time, to protect consumers and support regulatory work.

Today, heavy metals in cosmetics are mainly detected by inductively coupled plasma mass spectrometry (ICP-MS) and atomic absorption spectrometry (AAS). Both methods are accurate and sensitive, but they have clear drawbacks. ICP-MS instruments are expensive to buy and maintain, and samples must be digested with strong acids before analysis. AAS can only measure one element at a time and requires swapping hollow cathode lamps when switching between elements. These limitations make it hard to use them for large-scale screening or field testing. Laser-induced breakdown spectroscopy (LIBS), on the other hand, can detect multiple elements quickly with little or no sample preparation, and portable LIBS systems are already available [4,5]. LIBS has been used to detect heavy metals in many cosmetic products, including talcum powder [6], eyeliner [7], lipstick and eye shadow [8,9], face foundation [10], lip balms [11], personal care products [12], and hair dyes [13]. Liu et al. achieved sensitive detection of trace Pb and Cd in cosmetics by combining LIBS with ultrasound-assisted extraction, showing that a good sample introduction strategy can greatly improve LIBS results for complex samples [14]. However, applying LIBS directly to high-moisture, semi-solid products like hair dye creams is still very difficult. Water in the sample boils rapidly under laser irradiation, causing droplet splashing, unstable plasma, and even plasma shutdown, which leads to weak signals and poor reproducibility [14].

Fiber lasers are well-suited as LIBS excitation sources. They offer good beam quality, high repetition rates up to hundreds of kHz, compact size, stable output, and low operating costs, all of which make them attractive for portable systems [15]. Fiber laser LIBS has been used for quantitative analysis of steels [16], aluminum alloys [17,18], and copper alloys [19], and recent studies have looked at fiber-specific issues, such as elemental fractionation [20] and multi-laser parameter effects [21]. But fiber laser LIBS has not yet been applied to cosmetic products. The high water content and complex organic matrix of emulsion-type samples are very different from solid metals, and they bring new challenges for laser ablation and plasma formation.

To improve the detection sensitivity of LIBS for liquid and semi-solid samples, several enhancement strategies have been developed. Surface-enhanced LIBS (SEL) is a simple but effective approach where an aqueous sample is dropped onto a solid substrate and dried, converting the analytes from liquid into a solid residue that can be directly ablated [22,23]. This avoids the problems of direct liquid analysis, such as splashing and plasma quenching. Substrate engineering has further improved this approach. Superhydrophobic–hydrophilic patterned surfaces [24,25] and femtosecond laser-textured nanostructures [26,27] have been

used to control how droplets wet and dry, confining analytes into small concentrated zones and reducing the coffee-ring effect that causes uneven analyte distribution. Another approach, nanoparticle-enhanced LIBS (NELIBS), uses metallic nanoparticles (usually Au or Ag) deposited on the sample. When the laser hits these nanoparticles, they produce strong local electric field "hot spots" at particle gaps and sharp edges through localized surface plasmon resonance. These hot spots lower the ablation threshold and help the plasma form more easily, giving stronger signals [28,29]. A third approach, discharge-assisted LIBS, uses a high-voltage spark to add extra energy into the plasma right after the laser pulse. This promotes more collisions, ionization, and excitation of the ablated species, and extends the plasma lifetime. Signal enhancement factors of 10 to 100 times over single-pulse LIBS have been reported [30,31]. These three methods operate at different stages of the analytical process. SEL concentrates the analytes and removes the liquid matrix during sample preparation. NELIBS boosts ablation and plasma formation at the surface. Discharge-assisted LIBS reheats and sustains the plasma after ablation. Combining them could give much better results than any single method alone.

Despite good progress, there are still important gaps. First, most LIBS studies on cosmetics have focused on dry products like powders and lipsticks, while semi-solid emulsion products like hair dye creams, with high water content and complex organic matrices, have received much less attention. Second, although each enhancement technique (SEL, nanoparticle enhancement, discharge-assisted LIBS) has been demonstrated on its own, no one has combined them into one platform for cosmetic heavy metal detection. Third, fiber laser LIBS has never been tested on cosmetic products, so its performance for such samples has not been extensively investigated. This is because, although both sources operate at 1064 nm, the fiber laser delivers much longer pulses (~350 ns) than a standard Q-switched Nd:YAG laser (5–10 ns). This results in much lower peak irradiance and a more thermal ablation regime, all of which lead to ablation and plasma emission characteristics distinctly different from those of conventional Nd:YAG-based LIBS. To fill these gaps, this study develops a spark discharge-LIBS (SD-LIBS) system based on a fiber laser. The system combines a superhydrophobic–hydrophilic patterned graphite substrate and Au nanoparticle enhancement for the simultaneous detection of five heavy metal ions (Ag, Pb, Cd, As, Hg) in hair dye creams. A low-cost fiber laser (1064 nm, 350 ns pulse width) is used to make hydrophilic micro-pits on a superhydrophobic graphite surface. This patterned substrate traps and concentrates analyte residues inside the hydrophilic pits when the droplet dries. During measurement, a synchronized high-voltage discharge reheats and sustains the plasma, and Au nanoparticles provide additional LSPR-based enhancement. Key parameters including discharge capacitance and voltage, Au nanoparticle concentration, pit diameter, and sample volume were carefully optimized. The analytical performance was evaluated, and the method was validated by testing four commercial hair dye cream samples, using ICP-MS as a reference method.

2. Materials and Methods

2.1. Materials

The substrate material used in this study was high-purity graphite sheets with a purity of no less than 99.99% and dimensions of 20 × 20 mm with a thickness of 0.6 mm, purchased from Wenhou Metal Materials Co., Ltd., Hefei, China. Ultra Ever Dry solution, a commercial superhydrophobic coating material used to fabricate the superhydrophobic layer on the graphite substrate (see Section 2.3), and its dedicated spraying equipment were obtained from Dongguan Weijing Nano Materials Co., Ltd., Dongguan, China, DongguanE Single-element standard solutions of silver, arsenic, cadmium, chromium, and lead (concentration: 1000 μg/mL) were purchased from NCS Testing Technology Co., Ltd.,

Beijing, China. Gold nanoparticle solution with a particle size of 20 nm and a concentration of 50 mg/L was purchased from Xianfeng Nano Technology Co., Ltd., Nanjing, China. Electronic components for the discharge module, including capacitors and resistors, were purchas Shenzhen Wanjaer Electronics Co., Ltd., Shenzhen, China. Pure tungsten discharge needles (1.5 mm × 16 mm) were purchas Nangong Ruili Alloy Welding Materials Co., Ltd., Nangong, China. The hair dye cream samples were four different brands of unknown hair dye creams purchased from the Taobao e-commerce platform in China, numbered as Sample 1, Sample 2, Sample 3, and Sample 4 in order.

2.2. SD-LIBS Instrument System

A schematic of the SD-LIBS instrument used in this study is shown in Figure 1. The components and their sources are as follows: fiber laser (YDFLP-50-M8, Shenzhen Jeptron Photonics Co., Ltd., Shenzhen, China), short-pass dichroic mirror (DMSP1000T, cutoff wavelength 1000 nm, Thorlabs Photonics Technology Co., Ltd., Shanghai, China), near-infrared metallographic objective lens (magnification 20×, working distanceInfinity Optical Instrument Co., Ltd., Shanghai, China), YLE-2000-200mJ laser energy (Beijing Yanbang Technology Co., Ltd., Beijing, China), ring illumination module (WC-35, Shanghai Noriska Electronics Technology Co., Ltd., Shanghai, China), CCD imaging system (800-A, Sangzhou Lingdian Trading Co., Ltd., Guangzhou, China), manual Z-axis stage (LZ125-2, Shenzhen Huike Pneumatic Precision Machinery Co., Ltd., Shenzhen, China), motorized XY translation stage (XY-100, Beijing Jiangyun Optoelectronics Technology Co., Ltd., Beijing, China), 3000 V high-voltage discharge power supply (DW-P302-50F5D, Dongwen High-Voltage Power Supply (Tianjin) Co., Ltd., Tianjin, China), light-collection fiber (core diameter 600 μm, numerical aperture Shanghai Ruhai Optoelectronics Technology Co., Ltd., Shanghai, China), six-channel micro-spectrometer system (HS2048, spectral range 153–786 nm, slit width 10 μm, FWHM 0.16 nm, Shanghai Ruhai Optoelectronics Technology Co., Ltd., Shanghai, China), and a commercial electronic control card (Ezcad2, Beijing JCZ Technology Co., Ltd., Beijing, China).

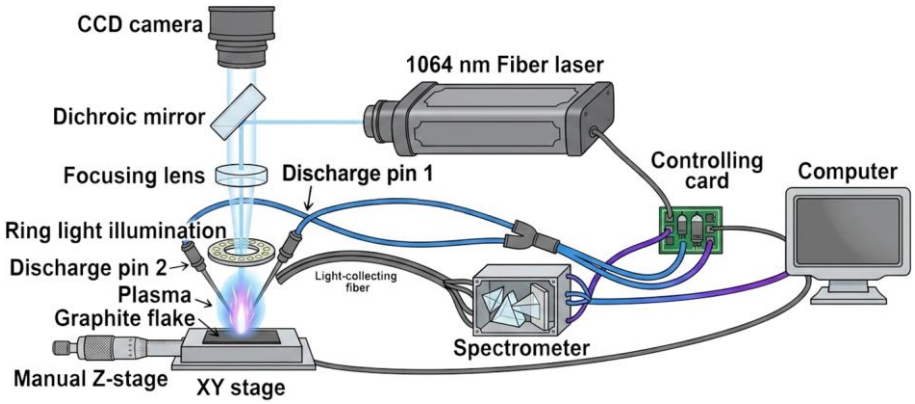


Figure 1. Schematic diagram of the SD-LIBS system utilized in this study.

The operation procedure of the instrument is as follows. The fiber laser emits a 1064 nm wavelength laser with a pulse width of 350 ns and a single-pulse energy of 2.82 mJ. To characterize the focused laser spot, single ablation pits were generated on the substrate under the same irradiation conditions and observed with a metallographic microscope (20× objective, MV3000, Jiangnan Yongxin Optical Co., Ltd., Nanjing, China), as shown in Figure 2. The mean pit diameter measured over ten parallel shots was 31.3 ± 2.0 μm, which was taken as the effective laser spot size on the surface, giving an average laser fluence of about 366 J/cm^2 (i.e., an average irradiance of about 1 GW/cm^2) at the sample surface. After being reflected by the dichroic mirror, the laser is focused onto the sample substrate

surface through the near-infrared metallographic objective. The system uses the ring illumination and CCD camera to precisely locate the hydrophilic pits and the laser focus on the sample. The illumination must be turned off before detection to prevent interference with spectral collection. The graphite substrate is fixed on the manual Z-axis stage (for calibrating laser focus) and the motorized XY translation stage (for moving and aligning the pits), allowing flexible position adjustment. At the moment when the laser pulse fires and generates plasma, the discharge needle above the laser ablation spot discharges synchronously. Because the laser power density in this experiment is relatively low (about 1 GW/cm^2, far below the several GW/cm^2 typically delivered by Q-switched Nd:YAG lasers), a light-collection fiber is placed beside the laser ablation spot (20 mm horizontally and 10 mm vertically away) to directly collect the plasma optical signal, which is then sent to the six-channel micro-spectrometer for spectral analysis. The synchronized operation of the entire system is controlled by a computer through the dedicated control card.

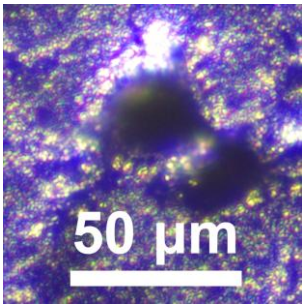


Figure 2. Representative surface morphology of a laser ablation pit on the graphite substrate, recorded with a metallographic microscope (20× objective). The mean pit diameter is 31.3 ± 2.0 μm (n = 10). Scale bar: 50 μm.

2.3. Preparation of Substrate and Samples

The substrate preparation involves three steps. First, the graphite substrate needs to be pre-treated: the graphite sheet is immersed in a 50% (*v*/*v*) ethanol-water solution and ultrasonically cleaned for 15 min, then taken out and dried in an oven at 70 °C. Next, the superhydrophobic coating is applied: the dried graphite sheet is aligned with its center 20 cm from the nozzle of the spray bottle and sprayed continuously with the Ultra Ever Dry solution for 3 s. The graphite sheet is then placed on a 60 °C electric heating plate to dry. After drying, a uniform superhydrophobic coating is formed on the graphite surface. Finally, the superhydrophobic graphite substrate is laid flat on the fiber laser engraving platform (YDFLP-E-30-M7, Shenzhen Jeptron Photonics Co., Ltd., Shenzhen, China). Using laser parameters of 1064 nm wavelength, 200 ns pulse width, and 0.8 mJ single-pulse energy, a high-speed galvanometer scanning system (10A, Shenzhen Zhibo Technology Co., Ltd., Shenzhen, China) performs raster laser scanning on the superhydrophobic graphite surface. This produces a 3 × 3 array of hydrophilic pits with 5 mm spacing between pit centers on the 20 mm × 20 mm superhydrophobic graphite surface. The pit diameters were 0.1, 0.2, 0.3, 0.4, and 0.5 mm, respectively. The metallographic microscope was used to photograph the cross-section of the superhydrophobic material-coated substrate and the hydrophilic pit sizes.

For sample preparation, 0.3 g of the sample is weighed accurately and diluted with 300 μL of water. The sample is then sonicated for 10 min, followed by centrifugation at 10,000 rpm for 20 min at room temperature. After the emulsion is broken, the clear liquid from the upper or lower layer is pipetted and dropped onto the hydrophilic pits. The entire substrate is then placed on a 60 °C electric heating plate to dry. The residue left after water evaporation is the sample to be tested.

2.4. Optimization of SD-LIBS Experimental Parameters

A schematic of the high-voltage discharge module constructed in this study is shown in Figure 3. R_1 is the current-limiting resistor. To protect the circuit, six 10 kΩ high-power resistors were connected in series so that the circuit current does not exceed the rated current of the high-voltage power supply (3000 V, 50 mA). C_1 is the capacitor. When the tungsten needle has not yet produced a spark discharge, the capacitor is in a charged state. When plasma is generated and the discharge circuit is completed, the electrical energy stored in the capacitor is released through the tungsten needle discharge. A probe connected across C_1 was connected to an oscilloscope (DS1202Z-E, RIGOL Technologies Co., Ltd., Suzhou, China) to monitor the discharge voltage. To measure the discharge current, a high-power R_2 resistor was placed in the direct discharge circuit, and a probe was connected across it to the same oscilloscope to measure its voltage. To minimize the effect of R_2 on the discharge circuit, its resistance was set to 1 Ω.

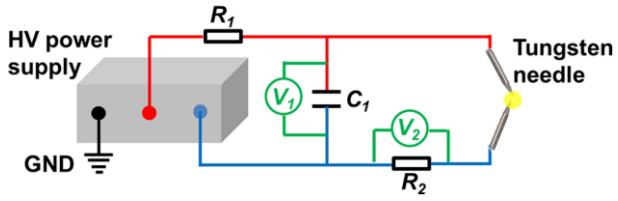


Figure 3. Schematic of the high-voltage discharge module.

To select the best discharge parameters, orthogonal experiments were performed on the capacitor C_1 and the discharge voltage. The capacitance values tested were 0.1, 0.22, 0.47, 1, 2.2, 3.3, 4.7, 6.8, 10, 15, 22, 33, 47, 68, 100, 150, 220, 330, 470, and 680 nF. The voltages tested were 1200, 1400, 1600, 1800, 2000, and 2200 V. Each experimental condition was repeated 50 times. After each measurement, the sampling position was refreshed by moving 0.5 mm using the motorized translation stage. During each measurement, spectral signals as well as discharge voltage and current signals were collected. The spectral acquisition delay was set to 1 μs, and the integration time was set to 10 ms.

To investigate the effect of gold nanoparticles on the detection results, the original gold nanoparticle solution with a concentration of 50 μg/mL was diluted to prepare solutions with concentrations of 1, 2, 5, 10, 20, and 50 μg/mL, respectively. A volume of 10 μL of each gold nanoparticle solution was pipetted and dropped onto the prepared hydrophilic pits. All subsequent procedures followed the same sample preparation steps described above.

To examine the effect of hydrophilic pit size and sample loading volume on signal intensity, orthogonal experiments were performed on these two factors. The pit diameters were 0.1, 0.2, 0.3, 0.4, and 0.5 mm, and the sample loading volumes were 5, 10, 15, 20, 25, and 30 μL. A volume of 10 μL of Pb standard solution was dropped onto the prepared hydrophilic pits. All subsequent procedures followed the same sample preparation steps described above.

2.5. ICP-MS/OES Experimental Method

Approximately 0.3 g of sample was weighed and placed in a clean polytetrafluoroethylene digestion vessel. A reagent blank was prepared at the same time. First, 7.0 mL of nitric acid and 2.0 mL of perchloric acid were added. The mixture was left overnight to allow sufficient reaction. Then, 1.0 mL of hydrogen peroxide was added, and the vessel was shaken several times to ensure the sample was fully submerged. The vessel was heated on a temperature-adjustable electric heating plate at 100 °C for about 30 min, then removed and cooled. The vessel lid was tightened, and the vessel was placed in a microwave diges-

tion system (REVO, Beijing Labtech Instrument Co., Ltd., Beijing, China). The maximum digestion temperature was 180 °C.

After digestion was complete, the vessel was removed and cooled, then opened. The digestion vessel containing the digested sample was placed on a temperature-adjustable electric heating plate at 100 °C for 10 min to remove excess nitrogen oxides from the sample, which could otherwise interfere with the measurement. The sample was transferred to a 25 mL volumetric flask with a stopper. The digestion vessel was rinsed twice with water, and the rinsing solutions were combined. The volume was adjusted to 25 mL with water. The sample was then transferred to a 50 mL centrifuge tube and centrifuged at 4000 r/min for 10 min. The supernatant was collected for analysis.

The detection of Pb, Cd, As, and Hg was performed using ICP-MS (7900, Agilent Technologies, Santa Clara, CA, USA). Instrument conditions were as follows: RF power: 1550 W; plasma gas flow rate: 15.0 L/min; auxiliary gas: 0.9 L/min; nebulizer gas flow rate: 0.85 L/min; number of analyses: 3, KED mode; He gas flow rate: 4.5 L/min; sampler and skimmer cones: platinum cones. The mixed calibration standard concentrations for As, Cd, Hg, and Pb were 0.0, 1.0, 5.0, 10.0, 50.0, and 100.0 μg/L. The detection of Ag was performed using ICP-OES (5100VDV, Agilent Technologies, Santa Clara, CA, USA). Instrument conditions were as follows: analytical line wavelength: 328.07 nm; plasma gas flow rate: 12 L/min; auxiliary gas flow rate: 1.00 L/min; nebulizer gas flow rate: 0.70 L/min; RF power: 1200 W; observation mode: radial; number of analyses: 3. The Ag calibration standard concentrations were 0.0, 1.0, 2.0, 5.0, 10.0, and 20.0 mg/L.

3. Results and Discussion

3.1. Superhydrophobic–Hydrophilic Structure and Spectral Data Preprocessing

In this study, a superhydrophobic–hydrophilic pit composite structure was prepared on the graphite sheet surface using graphite as the substrate. Figures 4a and 4b show the metallographic microscope images of the cross-section of the superhydrophobic layer and the hydrophilic pit, respectively. The light-colored regions in Figure 4b are the nanoparticle superhydrophobic coating prepared by the spraying method, and the dark-colored regions are the hydrophilic pits, which were fabricated by targeted nanosecond laser scanning ablation. To evaluate the batch-to-batch reproducibility of the substrate fabrication, five superhydrophobic–hydrophilic patterned substrates were independently prepared following the same procedure, with two replicate measurements on each substrate. The cross-sectional thickness of the superhydrophobic layer and the diameter of the hydrophilic pits were measured using a metallographic microscope. The results show that the superhydrophobic layer thickness is 63.6 ± 9.3 μm and the hydrophilic pit diameter is 96.5 ± 8.3 μm, indicating good reproducibility of the fabrication method. Figure 4c shows the side-view image of a 30 μL water droplet placed on the surface of this composite structure. The measured angle between the tangent line of the droplet and the substrate surface is 157.5°. Since this angle is greater than 150°, it indicates that the prepared coating has excellent superhydrophobic performance. At the same time, the hydrophilic pits can stably anchor the droplet in place, indicating that the superhydrophobic–hydrophilic composite structure prepared in this study can effectively meet the requirements of this experiment.

The raw spectral signal collected by the SD-LIBS system built in this experiment consists of three parts: the characteristic emission line signal of the analyte element, the continuous radiation background from the plasma, and the instrument noise. The plasma continuous radiation background forms a continuous baseline across the entire spectral range. This continuous background directly affects the true intensity of the characteristic spectral lines. In quantitative analysis, it usually causes the true intensity of the characteristic lines to be systematically overestimated, which reduces the analytical accuracy.

Therefore, before analyzing the characteristic line intensities, baseline correction must be applied to the raw spectrum to remove the interference from the continuous background on the subsequent qualitative and quantitative analysis. As shown by the blue raw spectrum in Figure 5a, the raw spectrum has a slowly rising continuous baseline across the entire wavelength range.

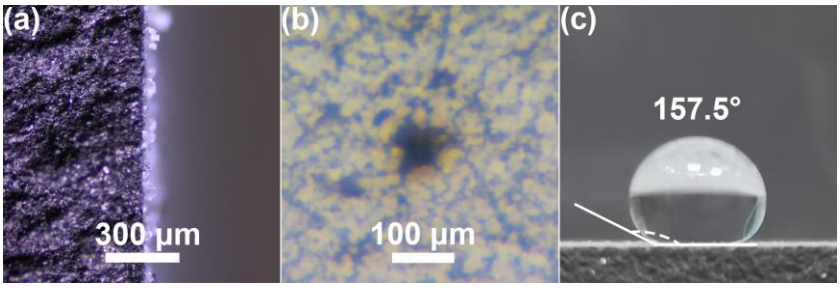


Figure 4. Characterization of the superhydrophobic–hydrophilic patterned graphite substrate. (**a**) Cross-sectional metallographic image of the superhydrophobic layer on the graphite substrate (scale bar: 300 μm). (**b**) Top-view metallographic image of a single hydrophilic pit (scale bar: 100 μm). (**c**) Water droplet (30 μL) on the composite surface, contact angle 157.5°.

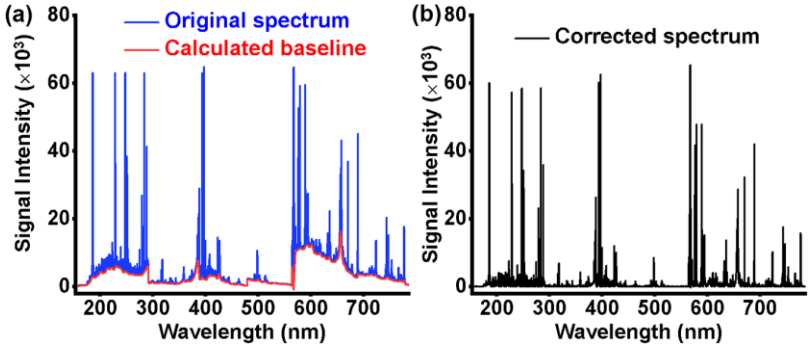


Figure 5. (**a**) Raw spectrum (blue) and fitted baseline (red); (**b**) spectrum after baseline correction.

All spectra in this study were processed using the Moving Window Minima Value algorithm developed by Yaroshchyk [32]. The basic principle of this algorithm is to set a sliding window whose width is slightly larger than the spectral peak width. The minimum value of all data points within the window is taken as the background estimate at the center of that window. As the window moves across the entire spectrum, a continuous baseline is generated. The core assumption is that sharp spectral peaks are superimposed on a slowly changing continuous background. The advantages of this algorithm are its simple and intuitive principle, high computational efficiency, and the ability to preserve the narrow LIBS peak signals as much as possible while removing the slowly drifting background. The red line in Figure 5a is the calculated fitted background. Figure 5b is the spectrum after baseline correction. After correction, the valley signals are right at zero on the vertical axis. The algorithm effectively separated and removed the continuous plasma background across the full wavelength range and fully preserved the characteristic peaks of both strong and weak elements, with no over-subtraction or peak distortion. The fitting results are objective with no manual intervention, which improves the reliability of LIBS spectral identification and quantitative analysis.

3.2. Effect of High-Voltage Discharge on Signal Intensity

To improve the radiation intensity of the laser-induced plasma, a high-voltage spark discharge module was added to the self-built LIBS system. Two tungsten needle electrodes

were placed symmetrically above the sample. When the laser pulse ablated the graphite substrate and formed the initial plasma, the discharge triggered as the plasma expanded into the electrode gap, injecting additional energy. This process intensifies collisional ionization and excitation among plasma species, greatly increasing the emission intensity of the analytical lines. Figure 6a compares the C I 283.6 nm line before and after discharge (22 nF, 2000 V). Without discharge, the peak intensity is below 500, nearly buried in the background noise. With discharge, the same line rises to nearly 60,000, a gain of about 120 times. This result confirms that the high-voltage discharge method provides substantial signal enhancement for LIBS signal enhancement.

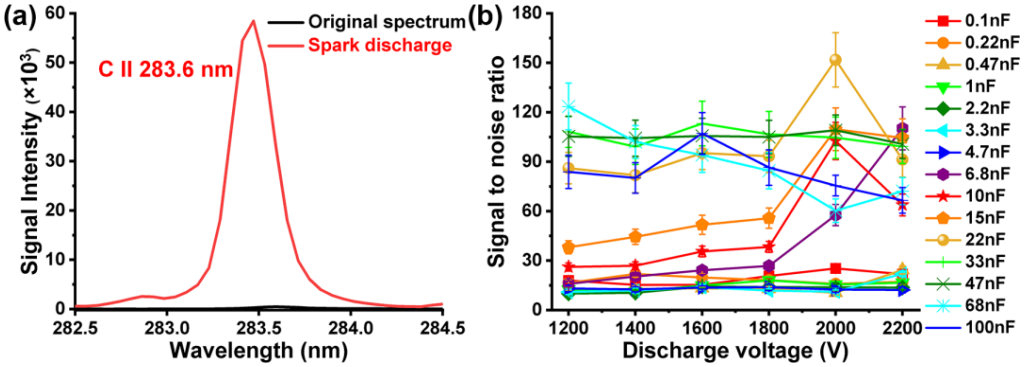


Figure 6. (**a**) Comparison of the C I 283.6 nm spectral line intensity before and after discharge (22 nF, 2000 V); (**b**) effect of different discharge parameters on the signal-to-noise ratio.

To find the optimal conditions, we examined the effects of capacitance and discharge voltage on the signal-to-noise ratio (SNR) of the C I 283.6 nm line. The laser energy and delay time were fixed, while capacitance was varied from 0.1 to 100 nF and voltage from 1200 to 2200 V. As shown in Figure 6b, the SNR trend with voltage is not monotonic. For small capacitances (0.1–4.7 nF), the SNR is low and increases only slightly with voltage. For medium capacitances (6.8–33 nF), the SNR rises clearly with voltage, peaking at 2000 V before dropping at 2200 V. For large capacitances (47–100 nF), the SNR is relatively high across the whole range but decreases gradually as voltage rises.

The distinct trends across the three capacitance ranges reflect the competition between signal enhancement and background radiation. A spark discharge boosts the characteristic line emission but also generates continuous background from bremsstrahlung and recombination [33,34]. For small capacitances (0.1–4.7 nF), the stored energy is at most tens of microjoules. The discharge is weak, so the signal gain is small and the additional background is negligible; the SNR stays low and changes little with voltage. For medium capacitances (6.8–33 nF), the stored energy reaches the millijoule range. The discharge effectively re-excites the plasma, and the signal enhancement clearly outweighs the background increase, yielding a strong SNR enhancement. At 2200 V, however, the discharge becomes excessive. The bremsstrahlung background grows disproportionately because it scales strongly with electron density and temperature [31], and the rising noise begins to offset the signal enhancement. For large capacitances (47–100 nF), the stored energy is even larger. The sustained discharge produces an intense background across the entire voltage range. In addition, extra emission lines from analyte elements, substrate impurities, and the tungsten electrode appear, causing spectral congestion that further raises the apparent noise near the target line. The net SNR therefore depends on whether the signal gain outpaces the combined increase in background and spectral interference.

Among all tested combinations, the maximum SNR of 151.7 was achieved at 22 nF and 2000 V, 12.4 times higher than without discharge. The voltage upper limit was set to 2200 V for two reasons. First, at excessively high voltages, the tungsten needle tip melts due to local overheating, introducing tungsten emission lines into the spectrum and interfering with measurement accuracy. Second, too high a voltage can cause the laser-induced plasma to bridge the electrode gap and trigger a self-sustaining arc discharge, which disrupts the analytical process [35]. Therefore, the optimal discharge parameters are 22 nF and 2000 V. Under these conditions, the discharge voltage and current waveforms (Figure 7) show an oscillatory mode lasting about 4.5 μs, with a peak power of 715 kW and total injected energy of 0.438 J. This oscillatory discharge gives the plasma multiple energy injections instead of one continuous heating event. Each cycle reheats the plasma, which prolongs the emission lifetime and enhances the spectral line intensity [30,34]. The injected energy of 0.438 J is much larger than the laser pulse energy of 2.82 mJ, indicating that the discharge provides the dominant energy input for signal enhancement.

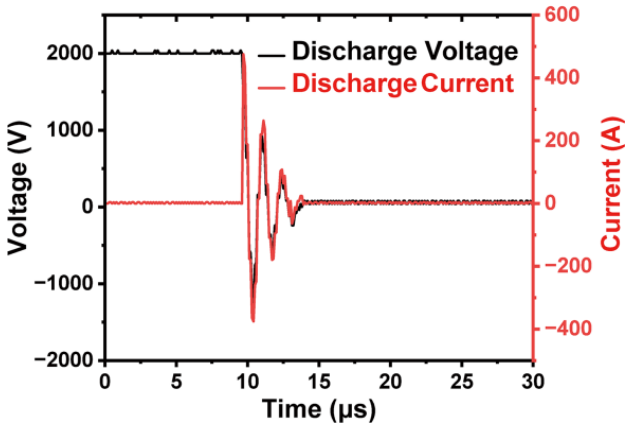


Figure 7. Dynamic discharge voltage and current waveforms at discharge parameters of 22 nF and 2000 V.

To evaluate the long-term stability of the discharge enhancement strategy, a 7-day continuous discharge experiment was conducted. Each day, 500 discharge-enhanced spectra of graphite were collected, corresponding to a throughput of more than 100 samples per working day, which represents typical daily laboratory usage. The signal intensity of the CN I line at 388.3 nm was monitored as the stability indicator. As shown in Figure 8, the normalized CN I 388.3 nm signal intensity exhibits a slight downward trend over 7 days, but the decrease remains within 10% of the initial value, demonstrating that the enhancement strategy maintains adequate performance for sustained analytical use. The gradual signal decrease is primarily attributed to the progressive wear of the tungsten discharge needle electrode during repeated sparking. Each discharge causes minor material loss at the needle tip, which slightly alters the discharge gap and plasma conditions over time. This is further supported by the weak W I emission line at 400.8 nm (Figure 8a), which indicates that the loss of tungsten material during spark discharge is slight but also inevitable. Nonetheless, the problem can be easily tackled by replacing a new pair of tungsten needles within one week.

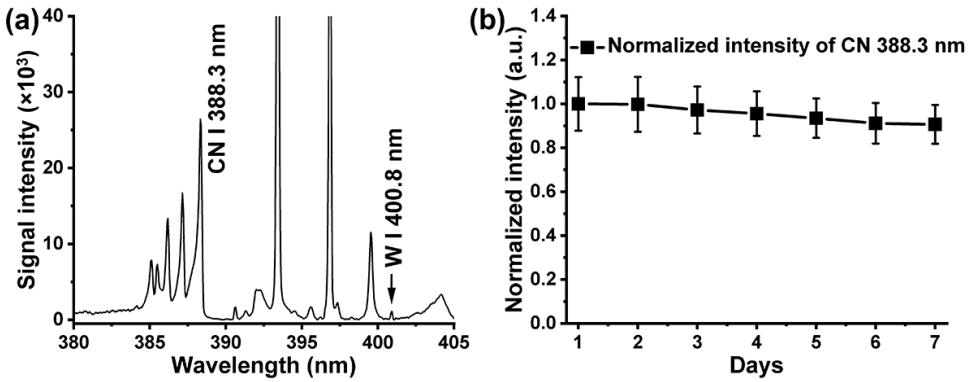


Figure 8. Long-term stability of the discharge enhancement strategy. (**a**) LIBS spectrum collected during the 7-day discharge stability test, showing the CN I 388.3 nm emission line and the W I 400.8 nm emission line from the tungsten discharge needle electrode. (**b**) Normalized intensity of the CN I 388.3 nm spectral line over 7 days (500 discharges per day). Error bars represent the standard deviation of 500 measurements per day.

3.3. Effect of Gold Nanoparticles on Analyte Signal

In addition to high-voltage discharge, previous studies have shown that gold nanoparticles deposited on the sample surface can also enhance LIBS signals [28,29]. The enhancement is mainly attributed to the localized surface plasmon resonance (LSPR) effect [28]. When the laser pulse strikes the nanoparticles, strong near-field enhancement produces hot spots in the gaps between particles and at sharp tips, where the local electric field can be several orders of magnitude higher than the incident field. The enhanced local electric field lowers the ablation threshold of the sample, so more material is removed and vaporized. The nanoparticles also act as nucleation sites for plasma formation, which speeds up plasma development and improves electron collisional excitation. Together, these effects significantly increase the emission intensity of the analytical lines. Gold nanoparticles are chemically stable and introduce little spectral interference, making them a commonly used enhancement medium in NELIBS experiments.

To test whether gold nanoparticles could improve the analytical performance of our system, we dropped 10 μL of gold nanoparticle solution at concentrations of 0, 1, 2, 5, 10, 20, and 50 mg/L onto the graphite substrate surface. After drying, LIBS spectra were collected under the same conditions. The signal intensity of the C I 283.66 nm line as a function of gold nanoparticle concentration is shown in Figure 9. Without gold nanoparticles, the signal intensity is 17,378. At 50 mg/L, the signal reaches 25,944, an enhancement of about 49.3%.

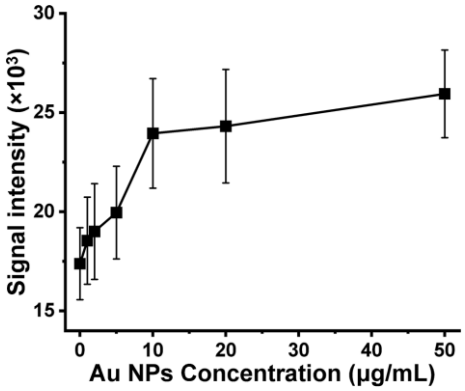


Figure 9. Effect of gold nanoparticle concentration on signal intensity.

Within the experimental concentration range, the signal intensity increases monotonically with gold nanoparticle concentration, but the rate of increase slows down by around 10 mg/L, indicating a tendency toward saturation. This saturation can be explained by several factors. First, as nanoparticle coverage increases, the electromagnetic coupling between neighboring particles begins to overlap. The enhanced area expands, but the peak local electric field does not increase linearly with particle coverage. The electromagnetic enhancement gradually saturates, so the signal enhancement slows down. Second, when the nanoparticle coverage is too high, part of the laser energy is absorbed and scattered by the dense nanoparticle layer, reducing the effective laser fluence that reaches the graphite substrate and thus limiting the amount of material ablated. Third, after drying, the nanoparticles may evolve from a well-dispersed monolayer to multilayer stacking and agglomeration. Well-dispersed nanoparticles are most favorable for field enhancement, while excessive agglomeration reduces the enhancement efficiency. In summary, gold nanoparticle enhancement contributed a 49.3% signal increase in this study.

3.4. Effect of Pit Size and Sample Loading Volume on Signal Intensity

To improve the signal intensity and ease of operation, we optimized two key parameters: pit diameter (0.1 to 0.5 mm) and sample loading volume (5 to 30 μL). The experimental data, shown in Figure 10, clearly reflect the effects of these two factors on signal intensity. The overall trend is that the signal intensity increases with larger sample loading volume and smaller pit diameter. Regarding pit size, smaller-diameter pits show a clear advantage under all sample loading conditions. This difference is due to the different degree of spatial enrichment of the solute after drying. On the superhydrophobic–hydrophilic substrate, the droplet is confined within the hydrophilic pit. Smaller pits effectively suppress the uneven solute distribution caused by the coffee-ring effect, so that after drying the analyte is concentrated in a very small ablation area. When the laser pulse fires, the smaller pit greatly increases the amount of sample ablated per unit area, and the density of analyte particles in the plasma increases accordingly, leading to a stronger signal. Regarding sample loading volume, the signal intensity increases steadily with larger volume, which is the natural result of increasing the total mass of analyte. However, the enhancement is not linear. Smaller pits benefit more from increasing the sample volume, while larger pits show relatively limited enhancement. This interaction effect further confirms the central role of spatial enrichment in achieving high-sensitivity detection. Simply increasing the analyte mass without effective spatial confinement cannot be fully converted into signal enhancement.

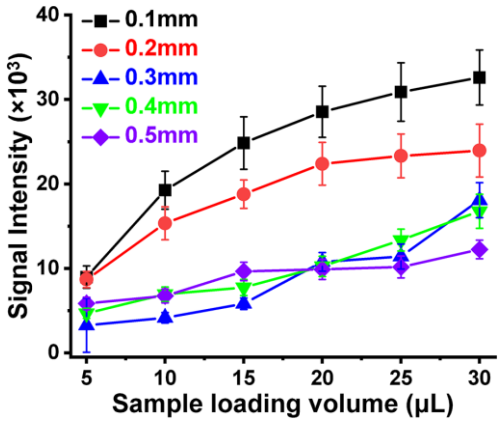


Figure 10. Effect of different sample loading volumes and pit diameters on signal intensity.

It should be noted that the upper limit of sample loading volume was set to 30 μL after balancing signal intensity and practical efficiency. First, the drying time of a 30 μL

droplet at 60 °C was measured to be about 13 min, which is relatively long. Additional tests showed that 50 μL and 100 μL droplets needed about 18 and 24 min to dry, obviously longer than the 13 min of the 30 μL case. Second, the graphite substrate used in this experiment has dimensions of 20 mm × 20 mm, with a 3 × 3 array of 9 detection points. At larger volumes the droplets on neighboring pits (5 mm apart) will occupy too much area and could easily merge with inappropriate sample loading operation. Considering signal enhancement, analytical efficiency, and array integration together, the optimal combination was determined to be a pit diameter of 0.1 mm with a sample loading volume of 30 μL. All subsequent quantitative experiments were conducted under these conditions.

3.5. Analytical Performance Evaluation

Through systematic optimization of the high-voltage discharge parameters, nanoparticle enhancement conditions, and pit diameter and sample loading volume on the superhydrophobic–hydrophilic patterned substrate, the optimal analytical conditions have been established. On this basis, this section further evaluates the actual analytical performance of the system for five target heavy metal elements in hair dye creams from four aspects: qualitative identification, quantitative linearity, method detection limit, and spiked recovery. To facilitate quantitative analysis, seven standard solutions at different concentrations were prepared (Table 1).

Table 1. Concentrations (μg/mL) of the five metal ions in the seven standard solutions.

	Ag	As	Cd	Hg	Pb
Standard 1	0.001	1	0.001	1	0.01
Standard 2	0.002	2	0.002	2	0.02
Standard 3	0.005	5	0.005	5	0.05
Standard 4	0.01	10	0.01	10	0.1
Standard 5	0.02	20	0.02	20	0.2
Standard 6	0.05	50	0.05	50	0.5
Standard 7	0.1	100	0.1	100	1

First, qualitative identification of the mixed standard solution was performed. Standard solution 4 was selected and placed in the optimized high-voltage discharge-enhanced LIBS system for spectral acquisition. Figure 11 shows the spectral comparison between this mixed standard and the blank graphite substrate. The blank substrate exhibits only a flat carbon background in the corresponding wavelength range. After introducing the mixed standard, clear characteristic emission peaks appear: Pb I 405.8 nm, Cd I 643.2 nm, As I 277.8 nm, Hg I 435.8 nm, and Ag I 328.1 nm. Each peak is clearly distinguishable from the nearby baseline, with symmetric peak shapes and no significant overlapping interference. This result confirms that the system can simultaneously identify five heavy metal elements.

Next, calibration curves and linearity evaluation were conducted. Seven groups of standard solutions with concentration gradients listed in Table 1 were prepared. Under the optimal experimental conditions, the characteristic spectral line intensity at each concentration point was collected, and partial least squares (PLS) regression was used to establish calibration curves for the five elements. The results are shown in Figure 12. The regression coefficients R^2 for all five elements are close to 0.99. This result indicates that the system has linear response for the five target elements within the selected concentration range.

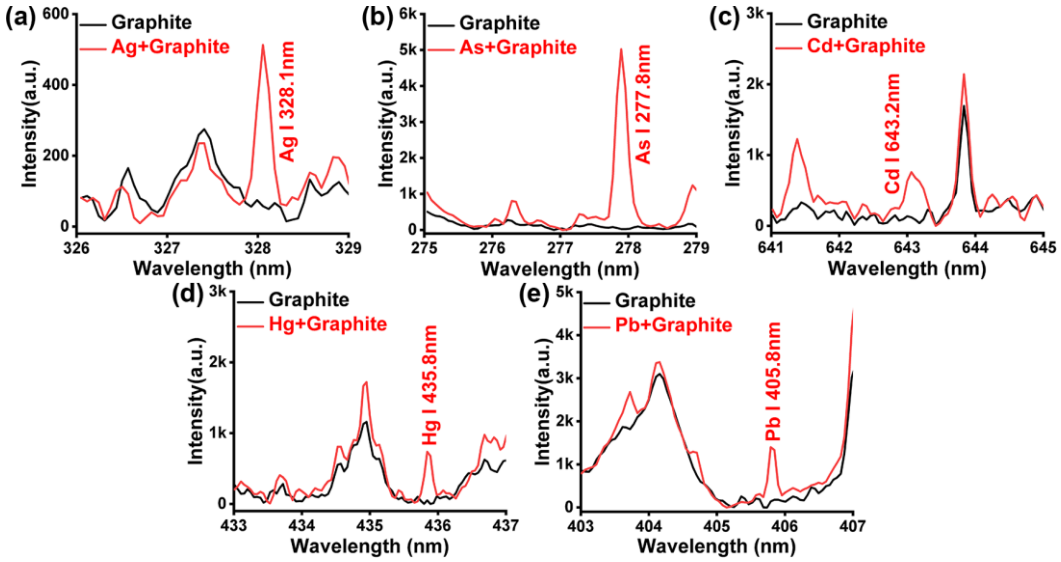


Figure 11. Characteristic spectral lines of the five metal elements (standard 4) on the graphite substrate. (**a**) Ag I 328.1 nm; (**b**) As I 277.8 nm; (**c**) Cd I 643.2 nm; (**d**) Hg I 435.8 nm; (**e**) Pb I 405.8nm.

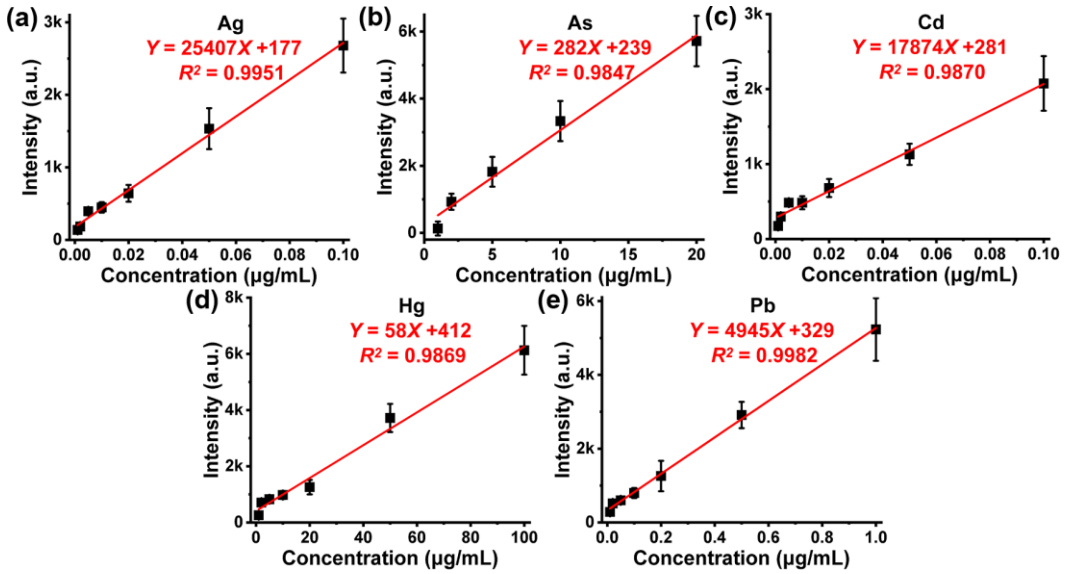


Figure 12. Calibration curves of the five elements at seven concentration levels. (**a**) Ag; (**b**) As; (**c**) Cd; (**d**) Hg; (**e**) Pb.

Subsequently, detection limits were calculated. Following the IUPAC-recommended 3σ criterion, the detection limit of each element was calculated according to the formula: LOD = 3 N/S, where N is the standard deviation of the background signal and S is the slope of the calibration curve. The results are summarized in Table 2. As shown in the table, the detection limits for Ag, As, Cd, Hg, and Pb are 1.9, 264.9, 4.1, 933.7 and 37.0 μg/L, respectively. The sample preparation procedure was as follows. A 0.3 g hair dye cream sample was weighed and diluted with 300 μL of deionized water, then subjected to ultrasonic extraction and centrifugal separation. Finally, 30 μL of the supernatant was taken for detection. The ratio of sample mass to extraction volume is approximately 1 g:1 mL, so the concentration actually detected by the instrument has an approximately 1:1 correspondence with the original content of the analyte in the sample. Therefore, the above detection limits can directly reflect the actual detection capability of the method for heavy metals in the sample. Among them, the detection limits of Cd and Ag have reached the

μg/L level, and even for Hg, which has the highest detection limit among the five elements, it is still below 1 μg/mL. Considering that the regulatory limits for heavy metals in hair dye creams are generally at the μg/mL level requested by various countries (for example, National Medical Products Administration of China), the detection limits of the system for all five elements are sufficient for practical detection. Moreover, we further calculated *SEE* (Standard Error of Estimate) and *RSE* (Relative Standard Error) to better evaluate the reliability of calibration curves. *SEE* is the standard error of estimate from linear regression, which can be calculated by the following equation:

$$SEE = \sqrt{\sum \frac{(y_i - \hat{y}_i)^2}{n-2}} \quad (1)$$

where y_i is the measured intensity and $\hat{y}_i$ is the predicted intensity according to the calibration curve. *RSE* can be calculated as: RSE = SEE/$\overline{y}$ × 100%, normalizing *SEE* against the mean signal intensity $\overline{y}$ for cross-element comparison. These two statistical values have been calculated for the five calibration curves and added to Table 2. As can be seen, the results are agreeable, indicating the reliability of the calibration curves.

Table 2. Analytical performance parameters of the five elements.

	Ag	As	Cd	Hg	Pb
S	25,407	282.29	17,874	58.48	4945
N	16.03	24.93	24.44	18.2	61.05
LOD (μg/L)	1.9	264.9	4.1	933.7	37.0
SEE *	71.3	902.8	82.0	269.2	83.7
RSE * (%)	8.30	12.56	10.78	13.58	5.05

* *SEE*: Standard Error of Estimate; *RSE*: Relative Standard Error.

Finally, recovery verification was performed. Two concentration levels were selected from the standard concentration gradients in Table 1 (Standard 2 as low concentration and Standard 5 as high concentration) for spiked recovery experiments. The results are listed in Table 3. Using the recovery data from Table 3, the predicted concentration for each spiked sample was back-calculated from the calibration curve, and the prediction error *RMSEP* (Root Mean Square Error of Prediction) was computed across both low and high spiking levels:

$$RMSEP = \sqrt{\sum \frac{(c_i - \hat{c}_i)^2}{N}} \quad (2)$$

where c_i is the accurate spiking level and $\hat{c}_i$ is the predicted concentration according to the calibration curve of certain element. Meanwhile, *RPE* (Relative Prediction Error) can be calculated by:

$$RPE = \frac{1}{2}\left(\frac{|c_{low} - \hat{c}_{low}|}{c_{low}} + \frac{\left|c_{high} - \hat{c}_{high}\right|}{c_{high}}\right) \times 100\% \quad (3)$$

The *RMSEP* values range from 0.0020 mg/L (Cd) to 3.02 mg/L (Hg), and the corresponding *RPE* values range from 10.28% (Cd) to 22.97% (Ag), which have been added to Table 3. These results confirm that the quantitative predictions of the method are reliable within the tested concentration ranges.

Table 3. Recoveries of the five elements.

	Ag	As	Cd	Hg	Pb
Recovery (low concentration)	74.71%	79.94%	93.41%	78.23%	80.37%
Recovery (high concentration)	79.35%	81.80%	86.04%	78.77%	88.06%
Average recovery	82.07%	82.07%	82.07%	82.07%	82.07%
RMSEP *	0.0029	2.59	0.0020	3.02	0.017
RPE * (%)	22.97	19.13	10.28	21.50	15.78

* *RMSEP*: Root Mean Square Error of Prediction; *RPE*: Relative Prediction Error.

However, the recoveries of the five elements at the low concentration level range from 74.7% to 93.4%, and at the high concentration level from 78.8% to 88.1%, with an overall average recovery of 82.07%. The recoveries are overall at an acceptable but slightly low level. Two main factors contribute to this result. The first factor is the limited extraction efficiency of the sample preparation method. Hair dye cream is a complex emulsion system containing oil phase components, surfactants, emulsifiers, organic dye molecules, and various functional additives. In this study, pure water was used as the sole extraction solvent, and the extraction relied on ultrasonic disruption and centrifugal phase separation. Although this process can break part of the emulsion structure, it cannot achieve complete demulsification. A portion of metal ions may remain entrapped within the oil phase or at the oil–water interface and is discarded together with the emulsion residue during centrifugation. More importantly, heavy metal ions in hair dye creams tend to form stable coordination compounds with organic dye molecules, particularly through functional groups, such as thiol and amino groups. These metal–organic complexes have low solubility in pure water, and the simple aqueous extraction used in this study cannot effectively break these coordination bonds. The variation in recovery among the five elements (Cd: 93.4%, Pb: 88.1%, As: 81.8%, Hg: 78.8%, Ag: 74.7%) may reflect differences in the affinity of each metal ion for the organic matrix components. In addition, the recoveries at the high concentration level are slightly higher than those at the low concentration level for most elements, suggesting that when the spiked amount increases, the aqueous extraction approaches its capacity limit, further supporting the conclusion that extraction efficiency is the primary limiting factor. The second factor is the matrix effect introduced by residual organic substances. Even after centrifugation, the aqueous phase supernatant still contains dissolved surfactants, emulsifiers, and small-molecule organic compounds. These residual organics are co-deposited with the target analytes on the hydrophilic pit during the drying step. During LIBS measurement, the organic matrix undergoes laser ablation along with the analytes, which can suppress the excitation efficiency of the target elements by consuming/scattering part of the laser energy. This matrix-induced signal suppression affects all five elements to a similar degree, which is consistent with the observation that the average recovery is approximately 82% for all elements. Nevertheless, an average recovery of about 82% is still within an acceptable range for a rapid screening-oriented detection method.

3.6. Determination of Hair Dye Cream Samples

To verify the detection reliability of the system in actual samples, four commercial hair dye cream products were selected and tested in parallel using the optimized SD-LIBS method and the ICP-MS/OES method. The results are summarized in Table 4. From the ICP-MS results, Cr was not detected in any of the four samples, indicating that chromium is absent or present at extremely low levels in this batch of hair dye cream products. For Pb, As, and Hg, the ICP-MS values in all four samples are below the detection limits of the system for these three heavy metals (Pb 0.037 μg/mL, As 0.265 μg/mL, Hg 0.934 μg/mL),

so no effective signals were obtained for these three elements in the LIBS detection, and the corresponding entries are marked as N.D. The LIBS spectra recorded from the four real samples around the characteristic lines of the five elements and other possible co-existing elements are provided as Figure 13, with the spectra of Samples 1–4 plotted together in each subfigure for direct comparison. The Ag I 328.1 nm line is clearly observed in Samples 1–3, including the 1000-fold diluted Samples 2 and 3 (Figure 13a), and is absent in Sample 4, while the As, Cd, Hg and Pb lines (Figure 13b–e) are not observed in any sample, consistent with the N.D. entries in Table 4.

Table 4. Comparison of the detection results of five heavy metal ions in four real hair dye cream samples by the proposed method and ICP-MS (mg/kg).

Samples	Samples	Ag	As	Cd	Hg	Pb
S_1	This study	0.156	N.D.	N.D.	N.D.	N.D.
S_1	ICP-MS/OES	0.186	0.013	N.D.	0.011	0.010
S_2	This study	22.989	N.D.	N.D.	N.D.	N.D.
S_2	ICP-MS/OES	19.467	0.014	N.D.	0.010	0.014
S_3	This study	10.364	N.D.	N.D.	N.D.	N.D.
S_3	ICP-MS/OES	9.029	0.013	N.D.	0.010	0.014
S_4	This study	N.D.	N.D.	N.D.	N.D.	N.D.
S_4	ICP-MS/OES	0.672	0.012	N.D.	0.009	0.005

N.D. means not detected.

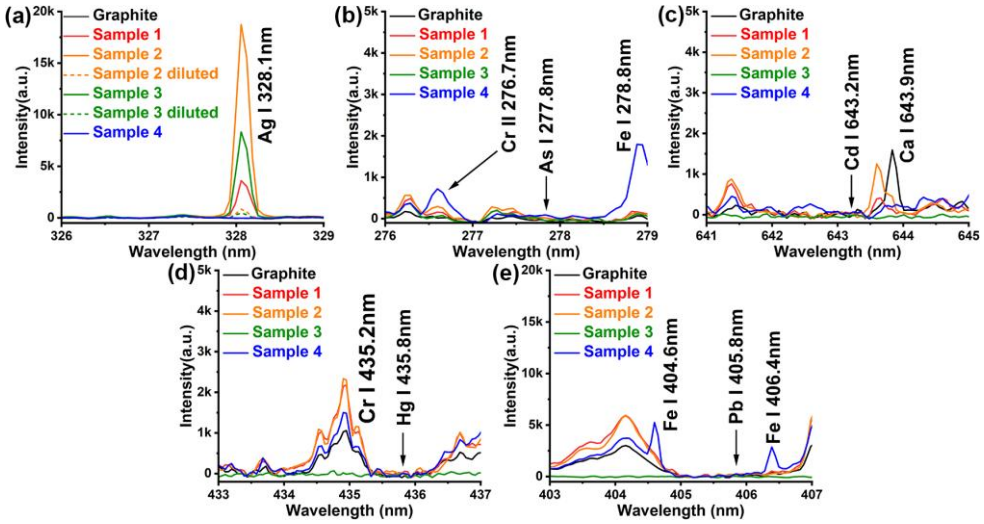


Figure 13. Spectra of Sample 1–4: (**a**) spectral segment indicating Ag I 328.1 nm, the dashed peaks were originated from 1000X dilution of Sample 2 and 3; (**b**) spectral segment indicating As I 277.8 nm; (**c**) spectral segment indicating Cd I 643.2 nm; (**d**) spectral segment indicating Hg I 435.81 nm; (**e**) spectral segment indicating Pb I 405.8 nm.

Ag is the core target element of this experiment. The ICP-OES results show that the Ag content is 0.186 mg/kg in Sample 1, 19.467 mg/kg in Sample 2, 9.029 mg/kg in Sample 3, and 0.672 mg/kg in Sample 4. The LIBS detection by the system successfully detected Ag signals in Samples 1, 2, and 3, with measured concentrations of 0.156 mg/kg, 22.989 mg/kg, and 10.364 mg/kg, respectively. From three replicate measurements, the relative standard deviations (RSD) for Samples 1, 2, and 3 are 14.1%, 12.6%, and 15.9%, respectively, with an average RSD of 14.2%. Using the ICP-MS/OES results as reference values, the accuracies for the three samples are 16.36%, 18.09%, and 14.78%, respectively, with an average error of 16.41%. The precision (RSD 12.6–15.9%) and accuracy (error 14.8–18.1%) of the system

for Ag detection are consistent across the tested concentration range (0.156–22.989 mg/kg), supporting the applicability of the method for real sample analysis.

Among these results, Sample 4 was confirmed by ICP-MS to contain 0.672 mg/kg of Ag, but no effective silver signal was obtained by the LIBS detection of the system. Through retrospective analysis of the experimental procedure, it was found that after pure water extraction of Sample 4, the extract showed abnormal viscosity. After loading onto the micropits of the graphite substrate and drying by heating, a gel-like film formed on the pit surface. The fiber laser used in this system has limited pulse energy and cannot effectively penetrate this gel-like layer to reach the analyte below. Laser ablation is therefore blocked and plasma cannot form normally, so no silver signal is detected. This phenomenon reveals the limitation of the pure water extraction method when dealing with complex sample matrices. The formulation differences among different brands of hair dye creams may cause certain excipients or thickeners to swell in the aqueous phase and form a gel, which interferes with the subsequent laser ablation process.

3.7. Comparison with Other Enhanced LIBS Techniques

To better assess the analytical capability of the proposed SD-LIBS system, Table 5 compares it with several recently reported enhanced LIBS techniques in terms of enhancement strategy, sample type, target elements, best detection limit, and enhancement factor. Shang et al. [36] used a micro-hole array sprayer to convert liquid samples into fine droplets on an organic membrane for dried-droplet analysis. It achieves LODs around 0.01 mg/L for six elements in water within 3 min, but lacks analyte preconcentration or plasma reheating, so its sensitivity is moderate. Xiao et al. [37] combines a slippery surface-aggregated substrate with Au NPs to suppress the coffee-ring effect and provide LSPR-based enhancement, reaching low microgram-per-liter LODs for Cu and Mn with a ~3× signal enhancement over the conventional dried droplet method. Wang et al. [38] used a sandpaper-polished metal substrate for surface-enhanced detection of heavy metals in water, achieving nanogram-per-milliliter LODs with a ~7× enhancement. While the substrate preparation is simple, it relies only on surface morphology and does not benefit from plasma reheating or nanoparticle assistance.

Table 5. Comparison of the proposed SD-LIBS with recently reported enhanced LIBS techniques.

References	Enhancement Strategy	Sample	Target Elements	Best LOD	Enhancement Factor
35	Micro-hole array sprayer + organic membrane	Water	Cu, Cd, Mn, Pb, Cr, Sr	0.01 mg/L	—
36	Slippery surface substrate + Au NPs	Water	Cu, Mn	3.72 µg/L	~3×
37	Sandpaper-polished metal substrate	Water	Pb, Cd, Cr	4.6 ng/mL	~7×
38	Electrodeposition + fs-laser + Ag NPs	Water	Cr, Pb, Cu	0.36 ng/mL	>100×
39	Electrodeposition + spark discharge	Water	Pb	0.15 ng/mL	~20×
40	Pulsed HV discharge (355 nm laser)	Kaolinite	Pb, Ba	45.6 ppm	7–10×
41	Arc discharge + fs-laser	Water	Cu	25 ng/mL	~7×
42	Quantum dots + double-pulse laser	Waste oil	Mg, Ca, Cr, Ba	0.02 ppm	~47×
This work	Spark discharge + Au NPs + superhydrophobic–hydrophilic substrate	Hair dye cream	Ag, Pb, Cd, As, Hg	1.9 µg/L	~12×

Methods combining electrodeposition with LIBS achieve much higher sensitivity. Chen et al. [39] first electrodeposits analytes onto a metal substrate, then applies Ag NP-enhanced femtosecond LIBS, reaching sub-ppb LODs (0.36 ng/mL for Cr) with an overall enhancement exceeding 100×. Wang et al. [40] combines electrodeposition with spark discharge and achieves a sub-ng/mL LOD for Pb with a ~20× enhancement. These methods offer excellent sensitivity, but the electrodeposition step adds 20–40 min and requires additional equipment, making them unsuitable for on-site use.

Among discharge-assisted methods, Zhang et al. [41] achieved 7–10× signal enhancement and reduced the Pb LOD from 98.3 to 45.6 ppm using a 355 nm laser with a 2 kV pulsed discharge. Yu et al. [42] reduced the LOD of Cu in water from 187 to 25 ng/mL (~7× enhancement) by coupling arc discharge with femtosecond laser ablation. Ding et al. [43] combines core–shell quantum dot enhancement with double-pulse excitation for waste oil analysis, achieving a 47× signal enhancement and ppm-level LODs, but requires synthesizing specialized quantum dots.

Compared with these methods, the proposed SD-LIBS system offers several practical advantages. First, it integrates spark discharge, Au NP enhancement, and superhydrophobic–hydrophilic substrate enrichment into a single platform, achieving low microgram-per-liter LODs while retaining multi-element capability. Second, the system is based on a low-cost fiber laser and standard electronic components, with hardware cost far below femtosecond laser systems. Third, the superhydrophobic coating is applied by simple spray coating, and the hydrophilic pits are fabricated by the same fiber laser used for detection. Fourth, sample preparation (water extraction, sonication, centrifugation) is straightforward, without electrodeposition or acid digestion. Fifth, the compact fiber laser and simple discharge circuit give the system clear potential for portable, on-site deployment. However, the method also has limitations. The LODs for As (264.9 μg/L) and Hg (933.7 μg/L) are higher than those of electrodeposition-based methods, limiting ultra-trace detection of these elements. The average recovery of 82.07% is somewhat low, mainly due to the extraction efficiency and matrix effect discussed above. The RSD of 14.2% is acceptable for screening but higher than methods with more controlled sample introduction. Additionally, the superhydrophobic coating may degrade over time, and some sample matrices can form gel-like films that block laser ablation. Future work could address these issues by introducing dilute acid-assisted extraction, exploring more durable coatings, and studying the synergistic mechanism between Au NPs and spark discharge.

4. Conclusions

In response to the demand for rapid detection of heavy metals in hair dye creams, this study designed and built a spark-discharge laser-induced breakdown spectroscopy system. Through systematic parameter optimization and method validation, high-sensitivity and rapid analysis of silver ions and multiple other target elements in hair dye cream samples was achieved, addressing the problems of complex pretreatment and high detection costs associated with conventional methods.

Regarding signal enhancement strategies, this study improved signal intensity through high-voltage discharge assistance and the addition of gold nanoparticles, and analyzed the mechanism of diminishing signal enhancement at high nanoparticle concentrations. The 0.1 mm micropit on the superhydrophobic–hydrophilic patterned graphite substrate combined with 30 μL sample loading effectively suppresses the coffee-ring effect while accommodating the requirements for drying time, substrate size, and rapid detection. In terms of analytical performance, the calibration curves for all five elements have R^2 values close to 0.99, and the detection limit reaches as low as 1.9 μg/L (Ag). After accounting for sample preparation, the detection limits can directly reflect the actual content in the

sample. The Ag detection results in real samples agree well with ICP-OES results, with an average accuracy of 16.41% and an RSD of 14.2%, validating the applicability of the method in complex matrices.

The main innovation of this study is a LIBS scheme that combines high-voltage discharge enhancement with superhydrophobic–hydrophilic substrate enrichment. Using low-cost hardware, it achieves detection sensitivity close to that of conventional large instruments, while meeting the practical needs for speed and convenience. In future work, the laser power can be increased to improve ablation of complex matrices. Dilute acid-assisted extraction or microfiltration can be introduced to improve recovery and anti-interference performance. The synergistic enhancement between gold nanoparticles and high-voltage discharge can also be explored to extend this method to more cosmetic, environmental, and food samples.

Supplementary Materials: The following supporting information can be downloaded at: https://www.mdpi.com/article/10.3390/photonics13090836/s1, Figure S1: (a) Spectra of Sample 1–4 indicating the signal of Ag I 328.1 nm. (b) Spectra of 1000 folds-diluted Sample 2 and Sample 3 indicating the signal of Ag I 328.1 nm; Figure S2: Spectra of Sample 1–4 indicating the signal of As I 277.8 nm; Figure S3: Spectra of Sample 1–4 indicating the signal of Cd I 643.2 nm; Figure S4: Spectra of Sample 1–4 indicating the signal of Hg I 435.8 nm; Figure S5: Spectra of Sample 1–4 indicating the signal of Pb I 405.8 nm.

Author Contributions: S.Z.: writing—original draft, supervision, methodology, formal analysis; J.L.: methodology; J.H.: methodology; Z.L.: methodology; F.C.: methodology; G.W.: writing—review and editing. All authors have read and agreed to the published version of the manuscript.

Funding: This research was funded by the Natural Science Foundation of Xiamen, China (Grant No. 3502Z202674002), Fujian-Taiwan Cosmetics Innovation and Testing Service Platform, Major Science and Technology Program of Xiamen Science and Technology Bureau, China (Grant No. 3502Z20241003), and the Xiamen Medical and Health Guided Project, China (Grant No. 3502Z20254ZD1228).

Institutional Review Board Statement: Not applicable.

Informed Consent Statement: Not applicable.

Data Availability Statement: The original contributions presented in this study are included in the article/supplementary material. Further inquiries can be directed to the corresponding author.

Conflicts of Interest: Zhisen Liang is the employee of Guangzhou Inspection, Testing and Certification Group Co., Ltd. The other authors declare no conflicts of interest.

References

1. Gyamfi, O.; Aboko, J.; Ankapong, E.; Marfo, J.T.; Awuah-Boateng, N.Y.; Sarpong, K.; Dartey, E. A systematic review of heavy metals contamination in cosmetics. *Cutan. Ocul. Toxico.* **2024**, *43*, 5–12. [CrossRef]
2. Molina-Hernandez, A.I.; Diaz-Gonzalez, J.M.; Saeb-Lima, M.; Dominguez-Cherit, J. Argyria after silver nitrate intake: Case report and brief review of literature. *Indian J. Dermatol.* **2015**, *60*, 520. [CrossRef]
3. *1223/2009*; Regulation (EC) No 1223/2009 of the European Parliament and of the Council of 30 November 2009 on Cosmetic Products (recast). European Parliament, Council of the European Union: Luxembourg, Luxembourg, 2009. Available online: https://eur-lex.europa.eu/legal-content/EN/ALL/?uri=celex%3A32009R1223 (accessed on 22 July 2026).
4. Gaudiuso, R.; Melikechi, N.; Abdel-Salam, Z.A.; Harith, M.A.; Palleschi, V.; Motto-Ros, V.; Busser, B. Laser-induced breakdown spectroscopy for human and animal health: A review. *Spectrochim. Acta Part B At. Spectrosc.* **2019**, *152*, 123–148. [CrossRef]
5. Guo, L.-B.; Zhang, D.; Sun, L.-X.; Yao, S.-C.; Zhang, L.; Wang, Z.-Z.; Wang, Q.-Q.; Ding, H.-B.; Lu, Y.; Hou, Z.-Y.; et al. Development in the application of laser-induced breakdown spectroscopy in recent years: A review. *Front. Phys.* **2021**, *16*, 22500. [CrossRef]
6. Gondal, M.A.; Dastageer, M.A.; Naqvi, A.A.; Isab, A.A.; Maganda, Y.W. Detection of toxic metals (lead and chromium) in talcum powder using laser induced breakdown spectroscopy. *Appl. Opt.* **2012**, *51*, 7395–7401. [CrossRef]

7. Gondal, M.A.; Dastageer, M.A.; Al-Adel, F.F.; Naqvi, A.A.; Habibullah, Y.B. Detection of highly toxic elements (lead and chromium) in commercially available eyeliner (kohl) using laser induced break down spectroscopy. *Opt. Laser Technol.* **2015**, *75*, 99–104. [CrossRef]
8. Augusto, A.d.S.; Batista, É.F.; Pereira-Filho, E.R. Direct chemical inspection of eye shadow and lipstick solid samples using laser-induced breakdown spectroscopy (LIBS) and chemometrics: Proposition of classification models. *Anal. Methods* **2016**, *8*, 5851–5860. [CrossRef]
9. Gondal, M.A.; Seddigi, Z.S.; Nasr, M.M.; Gondal, B. Spectroscopic detection of health hazardous contaminants in lipstick using Laser Induced Breakdown Spectroscopy. *J. Hazard. Mater.* **2010**, *175*, 726–732. [CrossRef]
10. Rehan, I.; Gondal, M.A.; Rehan, K.; Sultana, S. Spectral diagnosis of health hazardous toxins in face foundation powders using laser induced breakdown spectroscopy and inductively coupled plasma-optical emission spectroscopy (ICP-OES). *Talanta* **2020**, *217*, 121007. [CrossRef]
11. Nader, R.; Zoory, M.J.; Mohamad, H.J. Quantitative and qualitative analysis of lip balms in the Iraqi market using LIBS and concentration estimation based on electron density. *J. Opt.* **2024**, *55*, 2811–2817. [CrossRef]
12. Abrar, M.; Iqbal, T.; Fahad, M.; Andleeb, M.; Farooq, Z.; Afsheen, S. Determination of hazardous ingredients in personal care products using laser-induced breakdown spectroscopy. *Laser Phys.* **2018**, *28*, 056002. [CrossRef]
13. Gondal, M.A.; Maganda, Y.W.; Dastageer, M.A.; Al Adel, F.F.; Naqvi, A.A.; Qahtan, T.F. Detection of carcinogenic chromium in synthetic hair dyes using laser induced breakdown spectroscopy. *Appl. Opt.* **2014**, *53*, 1636–1643. [CrossRef]
14. Liu, Y.; Chu, Y.; Hu, Z.; Zhang, S.; Ma, S.; Khan, M.S.; Chen, F.; Zhang, D.; Guo, L.; Lau, C. High-sensitivity determination of trace lead and cadmium in cosmetics using laser-induced breakdown spectroscopy with ultrasound-assisted extraction. *Microchem. J.* **2020**, *158*, 105322. [CrossRef]
15. Gravel, J.-F.Y.; Doucet, F.R.; Bouchard, P.; Sabsabi, M. Evaluation of a compact high power pulsed fiber laser source for laser-induced breakdown spectroscopy. *J. Anal. At. Spectrom.* **2011**, *26*, 1354–1361. [CrossRef]
16. Zeng, Q.; Guo, L.; Li, X.; Shen, M.; Zhu, Y.; Li, J.; Yang, X.; Li, K.; Duan, J.; Zeng, X.; et al. Quantitative analyses of Mn, V, and Si elements in steels using a portable laser-induced breakdown spectroscopy system based on a fiber laser. *J. Anal. At. Spectrom.* **2016**, *31*, 767–772. [CrossRef]
17. Xu, Z.; Xu, B.; Peng, X.; Qin, Y.; Yan, X.; Liao, X.; Zhang, N.; Lai, Q.; Li, J.; Zhang, Q. Laser-ablation dependence of fiber-laser-based laser-induced breakdown spectroscopy for determining Cu, Mg, and Mn elements in aluminum alloys. *J. Anal. At. Spectrom.* **2021**, *36*, 2501–2508. [CrossRef]
18. He, X.; Li, R.; Chen, Y. Application of fiber optic high repetition rate laser-ablation spark-induced breakdown spectroscopy on the elemental analysis of aluminum alloys. *Appl. Opt.* **2019**, *58*, 8522–8528. [CrossRef]
19. Jiang, Y.; Li, R.; Chen, Y. Elemental analysis of copper alloys with laser-ablation spark-induced breakdown spectroscopy based on a fiber laser operated at 30 kHz pulse repetition rate. *J. Anal. At. Spectrom.* **2019**, *34*, 1838–1845. [CrossRef]
20. Zhang, S.; Xu, B.; Chen, F.; Chen, Y.; Wu, H.; Wang, G. Elemental fractionation effect in fiber laser induced breakdown spectroscopy. *Plasma Sci. Technol.* **2025**, *27*, 125505. [CrossRef]
21. Zhang, S.-D.; Xiao, Q.-T.; Chen, F.-F.; Chen, Y.-P.; Wu, H.-T.; Wang, G.-H. Multiple laser parametric study of fiber-laser-induced breakdown spectroscopy. *Appl. Opt.* **2025**, *64*, 1800–1808. [CrossRef]
22. Aguirre, M.A.; Legnaioli, S.; Almodóvar, F.; Hidalgo, M.; Palleschi, V.; Canals, A. Elemental analysis by surface-enhanced Laser-Induced Breakdown Spectroscopy combined with liquid–liquid microextraction. *Spectrochim. Acta Part B At. Spectrosc.* **2013**, *79–80*, 88–93. [CrossRef]
23. Yang, X.; Li, X.; Cui, Z.; Yao, G.; Zhou, Z.; Li, K. Improving the sensitivity of surface-enhanced laser-induced breakdown spectroscopy by repeating sample preparation. *Front. Phys.* **2020**, *8*, 194. [CrossRef]
24. Bae, D.-S.; Nam, S.-H.; Han, S.-H.; Yoo, J.-Y.; Lee, Y.-H. Spreading a water droplet on the laser-patterned silicon wafer substrate for surface-enhanced laser-induced breakdown spectroscopy. *Spectrochim. Acta Part B At. Spectrosc.* **2015**, *113*, 70–78. [CrossRef]
25. Yang, X.; Yi, R.; Li, X.; Cui, Z.; Lu, Y.; Hao, Z.; Huang, J.; Zhou, Z.; Yao, G.; Huang, W. Spreading a water droplet through filter paper on the metal substrate for surface-enhanced laser-induced breakdown spectroscopy. *Opt. Express* **2018**, *26*, 30456–30465. [CrossRef]
26. Chen, R.-B.; Fu, G.-R.; Li, H.-R.; Li, Y.; Wu, J.; Deng, G.-L.; Zhou, H.; Sui, X.-L.; Zhou, S.-H. Femtosecond laser-induced surface nanostructures for enhanced trace metal element detection in water. *Opt. Express* **2024**, *32*, 32849–32860. [CrossRef]
27. Ahlawat, S.; Mukhopadhyay, P.K.; Singh, R.; Dixit, S.K.; Bindra, K.S. Laser textured superhydrophilic silicon for uniform solidification and sensitive detection of water based samples using laser induced breakdown spectroscopy. *J. Anal. At. Spectrom.* **2023**, *38*, 883–892. [CrossRef]
28. Wang, Q.-Y.; Liu, Y.-T.; Jiang, L.-Y.; Chen, A.-M.; Han, J.-H.; Jin, M.-X. Metal micro/nanostructure enhanced laser-induced breakdown spectroscopy. *Anal. Chim. Acta* **2023**, *1241*, 340802. [CrossRef]
29. Yuan, L.; Wang, Q.-Y.; Yu, H.-L.; Lang, P.; Li, H.; Gao, X.; Lin, J.-Q. High-sensitivity determination of heavy metal elements in water with circular grooves and nanoparticle-enhanced LIBS. *J. Anal. At. Spectrom.* **2024**, *39*, 2097–2105. [CrossRef]

30. Khan, F.W.; Ahmed, N.; Baig, M.A.; Hedwig, R.; Pardede, M.; Kurniawan, K.H.; Tanra, I.; Karnadi, I.; Ahmed, R. Modification of plasma evolution dynamics in LIBS via spark discharge assistance for sub-ppm detection of heavy metals in aluminum alloys. *Spectrochim. Acta Part B At. Spectrosc.* **2026**, *242*, 107545. [CrossRef]
31. Robledo-Martínez, A.; Sobral, H.M.; García-Villarreal, L.A. Signal enhancement in laser-induced breakdown spectroscopy using gated high-voltage pulses. *IEEE Trans. Plasma Sci.* **2018**, *46*, 2392–2396. [CrossRef]
32. Yaroshchyk, P.; Eberhardt, J.E. Automatic correction of continuum background in Laser-induced Breakdown Spectroscopy using a model-free algorithm. *Spectrochim. Acta Part B At. Spectrosc.* **2014**, *99*, 138–149. [CrossRef]
33. Hou, Z.; Wang, Z.; Liu, J.; Ni, W.; Li, Z. Combination of cylindrical confinement and spark discharge for signal improvement using laser induced breakdown spectroscopy. *Opt. Express* **2014**, *22*, 12909–12914. [CrossRef]
34. Sobral, H.; Quintana-Silva, G.; Robledo-Martinez, A. Time-resolved optical characterization of the interaction between a laser produced plasma and a spark discharge. *Spectrochim. Acta Part B At. Spectrosc.* **2020**, *167*, 105844. [CrossRef]
35. Yang, W.M.; Zhu, R.; Zhang, C.; Liu, B.Y. Self-sustaining discharges in needle-to-plane geometry with hundreds of microns electrode gaps. *J. Electrostat.* **2017**, *87*, 236–242. [CrossRef]
36. Shang, J.; Ling, Y.; Ping, L.; Pan, K.; Xue, Y.; Wang, Y.; Li, J.; Zhang, S.; Zhong, S. Micro-hole array sprayer combined with an organic membrane to assist LIBS (MASOM-LIBS): A novel highly sensitive detection method for dissolved trace heavy metals in water. *Talanta* **2023**, *264*, 124780. [CrossRef]
37. Xiao, S.; Liu, Y.; Luo, Y.; Zhu, Y.; Wang, W.; Nie, J.; Huang, W.; Niu, C.; Gong, A.; Guo, L. Sensitivity and stability improvement on slippery surface-aggregated substrate for trace heavy metals detection using NELIBS. *Talanta* **2024**, *275*, 126001. [CrossRef]
38. Wang, Q.; Gao, X.; Wang, Z.; Cui, Y.; Chen, A.; Han, X. High sensitivity detection of heavy metal elements in water by polishing assisted SE-LIBS. *J. Anal. At. Spectrom.* **2025**, *40*, 1411–1418. [CrossRef]
39. Chen, Y.; Si, J.; Wan, X.; Wang, Y.; Chen, A.; Jin, M. Sub-ppb detection limit of Cr, Pb, and Cu in water by surface-enhanced LIBS with femtosecond laser. *Spectrochim. Acta Part B At. Spectrosc.* **2024**, *213*, 106880. [CrossRef]
40. Wang, Q.; Chen, A.; Chen, Y.; Jiang, Y.; Li, S.; Jin, M. Highly sensitive analysis of trace Pb in aqueous solution using electrodeposition and spark-discharge assisted laser-induced breakdown spectroscopy. *J. Anal. At. Spectrom.* **2021**, *36*, 1889–1894. [CrossRef]
41. Zhang, Y.; Wang, J.; Jin, X.; Zhu, H.; Su, X.; Qiu, R.; Zhou, Q.; Gu, Z.; Li, R.; Lü, T. Signal-enhancement mechanisms of Al and Pb in kaolinite by discharge-assisted LIBS. *J. Phys. D. Appl. Phys.* **2026**, *59*, 155201. [CrossRef]
42. Yu, X.; Jiang, Y.; Qi, H.; Han, J.; Chen, A.; Jin, M. Arc discharge-assisted enhancement of femtosecond LIBS for improved sensitivity in trace Cu detection in aqueous solutions. *Spectrochim. Acta Part B At. Spectrosc.* **2026**, *237*, 107445. [CrossRef]
43. Ding, W.; Xu, S.; Wang, T.; Pan, C.; Wang, X.; Fang, J.; Xia, Y.; Ma, S.; Hu, Y. Double-pulse laser-induced breakdown spectroscopy assisted by quantum dots for quantification of trace metals in waste oil. *Talanta* **2027**, *312*, 130309. [CrossRef]

Disclaimer/Publisher's Note: The statements, opinions and data contained in all publications are solely those of the individual author(s) and contributor(s) and not of MDPI and/or the editor(s). MDPI and/or the editor(s) disclaim responsibility for any injury to people or property resulting from any ideas, methods, instructions or products referred to in the content.